The Occurrence, Drivers, and Implications of Submesoscale Eddies on the Martha's Vineyard Inner Shelf

ANTHONY KIRINCICH

Woods Hole Oceanographic Institution, Woods Hole, Massachusetts.

(Manuscript received 6 October 2015, in final form 23 May 2016)

ABSTRACT

The occurrence, drivers, and implications of small-scale O(2–5) km diameter coherent vortices, referred to as submesoscale eddies, over the inner shelf south of Martha's Vineyard, Massachusetts, are examined using high-frequency (HF), radar-based, high-resolution (400 m) observations of surface currents. Within the 300 km^2 study area, eddies occurred at rates of 1 and 4 day^{-1} in winter and summer, respectively. Most were less than 5 h in duration, smaller than 4 km in diameter, and rotated less than once over their lifespan; 60% of the eddies formed along the eastern edge of study area, adjacent to Wasque Shoal, and moved westward into the interior, often with relative vorticity greater than f. Eddy generation was linked to vortex stretching on the ebb and flood tide as well as the interaction of the spatially variable tide and the wind-driven currents; however, these features had complex patterns of surface divergence and stretching. Eddies located away from Wasque Shoal were related to the movement of wind-driven surface currents, as wind direction controlled where eddies formed as well as density effects. Using an analysis of particles advected within the radar-based surface currents, the observed eddies were found to be generally leaky, losing 60%–80% of particles over their lifespan, but still more retentive than the background flow. As a result, the combined translation and rotational effects of the observed eddies were an important source of lateral exchange for surface waters over the inner shelf.

1. Introduction

Little is known about the role of lateral variability in the inner part of the continental shelf (Lentz and Fewings 2012), where upwelling or downwelling due to the coastal boundary condition occurs and surface and bottom boundary layers overlap and interact, generally in water depths of 10–50 m (Lentz 2001). A key link in the exchange between land and the larger ocean offshore, the inner shelf is forced by a variety of processes, including winds, waves, tides, and buoyant plumes, that generally define the character of circulation and control the stratification present (Austin and Lentz 2002; Tilburg 2003; Lentz et al. 2008). However, as the coast is approached, the effectiveness of these mechanisms, that is, along-shelf wind forcing, in driving across-shelf exchange decreases (Fewings et al. 2008). Thus, the effect of lateral stirring due to coherent features such as eddies, squirts, or jets could play a more important role in setting or maintaining the exchange present in the shallower-water depths of the inner shelf then farther offshore. Yet, even a basic characterization of the features present at scales smaller than 10 km, potentially driven by local bathymetric (i.e., Geyer and Signell 1990; McCabe et al. 2006; Checkley and Barth 2009) or baroclinic processes (i.e., McWilliams 1985), is unknown in most coastal areas.

This work uses the results of a novel deployment of high-frequency (HF) radar to investigate the occurrence and drivers of small-scale O(2–5) km diameter coherent vortices, referred to here as submesoscale eddies, south of Martha's Vineyard, Massachusetts, in order to begin to assess their potential impact on exchange. In general, across-shelf exchange controls the hydrographic structure of the coastal ocean as well as the across-shelf fluxes of nutrients and pollutants. Thus, the total exchange rates and their time dependence play a critical role in determining the productivity of the coastal ocean and the potential effects of harmful algal blooms (HABs) or offshore spills. Previous efforts documenting the exchange driven by along-shelf winds (Lentz 2001; Kirincich et al. 2005), across-shelf winds (Tilburg 2003; Fewings et al. 2008), and surface gravity waves (Lentz

Corresponding author address: Anthony Kirincich, Department of Physical Oceanography, Woods Hole Oceanographic Institution, 266 Woods Hole Rd., Woods Hole, MA 02543.
E-mail: akirincich@whoi.edu

DOI: 10.1175/JPO-D-15-0191.1

et al. 2008; Kirincich et al. 2009) have expanded our understanding of exchange, but only in the framework of along-shelf uniform forcings and depth-dependent responses. In contrast, even small variations in along-shelf bathymetry or background currents have been shown to cause significant exchange or export across the shelf in many coastal areas. Model and observational studies of the Mid-Atlantic Bight (Song et al. 2001; Tilburg and Garvine 2003; Yankovsky and Chapman 1995) found that bathymetric variability in the inner shelf led to the formation of upwelling centers and spatially variable exchange despite uniform winds. At larger scales, capes or seamounts have been shown to eject water masses and materials from the shelf due to the offshore flow of the along-shelf current (Barth et al. 2005; Castelao and Barth 2006). Variable, in time and space, buoyancy effects and winds have also been tied to both subtidal and seasonal spatially variable responses (Chant 2004; Kirincich and Barth 2009; Kohut et al. 2004).

A number of techniques have been developed specifically for detecting the surface signature of eddies in oceanic settings [see reviews by Chaigneau et al. (2008), Chelton et al. (2011), and Kim (2010)]. Most follow either vorticity-based arguments, for example, the Okubo–Weiss criterion (Okubo 1970; Weiss 1991), also known as the rate of deformation tensor, or the winding angle method (Sadarjoren and Post 2000), which looks for groups of almost closed streamlines to detect coherent features in the velocity field. Using HF radar data, Kim (2010) applied the winding angle method to a velocity streamfunction computed using an estimate of the nondivergent component of the surface currents, while Nencioli et al. (2010) used vector geometry and tuned eddy detection parameters to find the center of the eddy before estimating its size using the winding angle method. Estimates of the Lagrangian coherent structures (LCSs) present in HF radar velocities have also been used to delineate trapped cores of fluid as well as barriers to exchange (Lekien et al. 2005; Olascoaga et al. 2006; Lekien and Ross 2010). Using these approaches on the results of 2–3-km-resolution, 11–13-MHz radar systems, Beckenbach and Washburn (2004) and Nencioli et al. (2010) revealed sequences of mesoscale O(30–40) km vortices propagating westward through the Santa Barbara Channel due to both trapped coastal and topographic waves. With similar instrument resolution, Parks et al. (2009) found that topographic forcing drove mesoscale eddy formation along the Florida Current offshore of Miami. Using higher, 1-km resolution observations offshore of San Diego, California, Kim (2010) documented the occurrence of smaller O(5–15) km diameter eddies with O(1) Rossby numbers and strong vertical motions, assessed via the observed divergence of the surface currents, that were able to persist for days to weeks. Along with the larger flow field in which they are embedded, these submesoscale features [see Mahadevan and Tandon (2006) for a definition] have the potential to contribute substantively to the exchange of materials as well as the dissipation of energy (Capet et al. 2008) over the shelf.

This study uses observations of surface currents made at horizontal resolutions approaching 400 m via a unique installation of HF radar systems (Kirincich et al. 2013) to document the occurrence, drivers, and implications of submesoscale eddies over the inner shelf south of Martha's Vineyard, Massachusetts. Located along the southern New England shelf (Fig. 1), recent work in the area has documented startling examples of spatially variable circulation (Ganju et al. 2011; Kirincich et al. 2013) in an area where the depth-dependent exchange dynamics were thought to be remarkably consistent with simple, two-dimensional, along-shelf uniform theory (Lentz et al. 2008; Fewings et al. 2008). Based on high-resolution numerical model output, Ganju et al. (2011) suggested that significant spatial variations in the low-frequency (monthly to annually averaged) circulation existed that were previously unresolved by traditional observational methods and standard resolution models. Using high-resolution observations of surface currents, Kirincich et al. (2013) both validated the results of Ganju et al. (2011) and documented the impact of spatial variability on the inner shelf heat budget. While providing a context for the present work, previous HF radar-based analysis of coherent eddies has focused on features longer than 1 (Kim 2010) to 4 (Nencioli et al. 2010) days and larger than 5-km resolution. However, as the coastline is approached and the bottom shoals within the inner shelf, the temporal and spatial scales of coherent features should become smaller in size and potentially more transient in time. Thus, this study aims to document the full range of features present over the inner shelf.

The manuscript is organized as follows: The HF radar observations and study area are described first followed by the analysis methods utilized, including the identification and tracking of eddies, use of the depth-averaged vorticity equation as a diagnostic for eddy generation, and the advection of particles within the surface current observations. Results on the statistics, drivers, and secondary circulation are presented next, followed by an analysis of the implications for lateral exchange and a discussion of the key findings before conclusions are given.

2. Data and methods

a. *Surface currents*

Surface current observations were obtained by a system of three 25.5-MHz Coastal Ocean Dynamics Applications

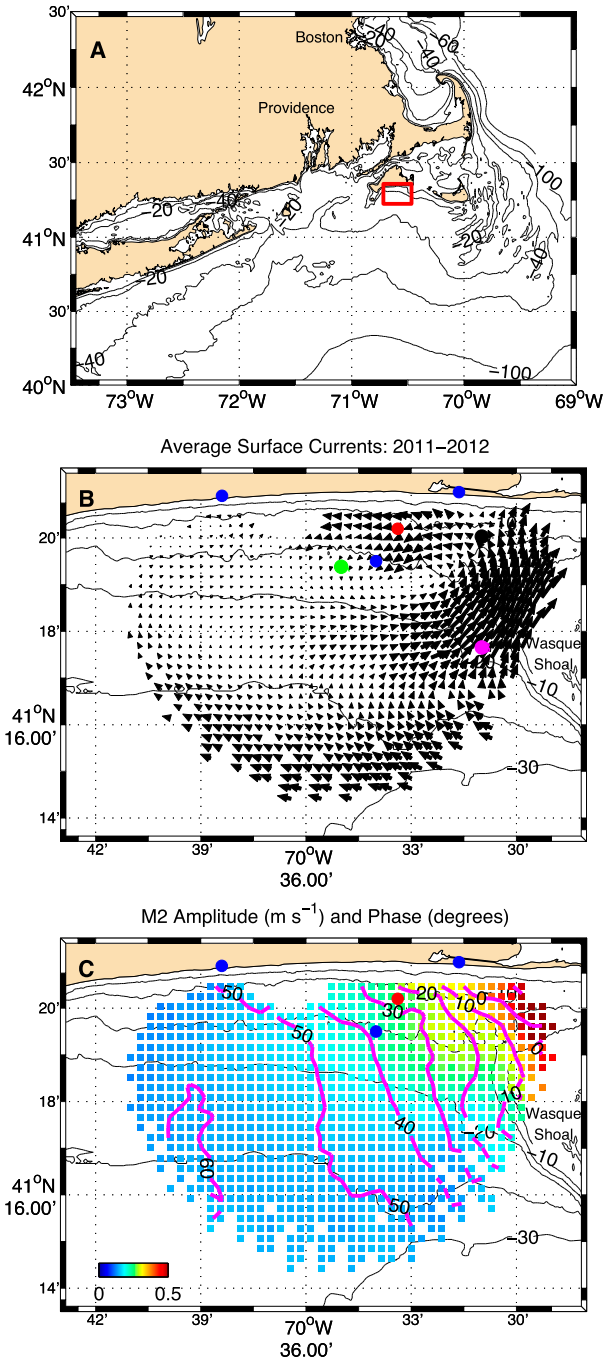

FIG. 1. (a) The southern New England shelf and the study area, outlined in red, offshore of the island of Martha's Vineyard. (b) HF radar site locations (blue) and in situ ADCP (red) with mean surface currents (black) calculated over the 18-month study period along with the locations of stations A (green), B (magenta), and C (black), used to show the average tidal velocities in Fig. 8. (c) The amplitude (shading) and phase (contours) of the M_2 tidal constituent, estimated at each grid point using T_tide.

Radar (CODAR) Ocean Sensor SeaSonde-type HF radars, measuring the top 0.5 m (Stewart and Joy 1974) and configured for high-resolution (~400 m) coverage within a 300 km^2 domain south of Martha's Vineyard and high accuracy (Kirincich et al. 2012, 2013; Rypina et al. 2014). High resolution and accuracy were achieved in three ways: First, radars were placed in close proximity, with two land-based systems approximately 10 km apart (Fig. 1b) and a third 4 km offshore on the Martha's Vineyard Coastal Observatory (MVCO) Air–Sea Interaction Tower (ASIT; Fig. 1b), and were operated on a common transmit bandwidth of 350 kHz, enabling range resolution of 429 m. Second, long (1024 point or ~8 min) spectral estimates of the radar backscatter were used to resolve Doppler velocities less than 0.01 m s^{-1}. Third, the radar backscatter observations were processed using the methods described in Kirincich et al. (2012) that result in higher-quality, reduced error estimates of surface currents relative to standard methods (Kirincich et al. 2012; de Paolo et al. 2015).

During an 18-month period spanning from 1 February 2011 to 31 July 2012, radial velocities from all sites were produced every 15 min, encompassing three successive spectral estimates of the radar cross section, and spatially averaged to 5° azimuthal bins. Vector surface currents were estimated for each point on a regularly spaced 400-m grid using all radials within 400 m and ±15 min every 30 min. The resulting dataset was further limited to include spatial locations with data-based geometric dilution of precision (GDOP) less than 1.75 (Chapman et al. 1997), data coverage greater than 50%, and screened for outliers following Halle (2008). Observations of winds during the study period were obtained from MVCO. Direct comparisons of this quality controlled data product to in situ MVCO-based ADCP observations yielded accuracy estimates of 0.05 m s^{-1} (Kirincich et al. 2013), measured as rms differences with in situ ADCP measurements 2 m deep. Further comparisons between drifter trajectories and those estimated from the Eulerian radar surface currents had mean separation speeds of 2.8 cm s^{-1} over a period of 12 h (Rypina et al. 2014).

Recent studies focused on the inner shelf south of Martha's Vineyard have documented strong gradients in the phase and amplitude of tidal velocities as well as a spatially variable background circulation (Ganju et al. 2011; Kirincich et al. 2013; Fig. 1b). To separate tidal velocities from both the lower- and higher-frequency variability, tidal fits were computed separately for each grid point over the study period using the T_tide (Pawlowicz et al. 2002) software package, applying harmonic fits only to constituents with periods less than

2 days and signal-to-noise ratios greater than 2. Dominating the estimated tidal constituents, the amplitude of the M_2 tide increases from 0.1 to 0.5 m s^{-1} over an alongshelf distance of 20 km with phase variations up to 60° (Fig. 1c). The spatial structure of the tide is due to the presence of Wasque Shoal located to the east of the radar domain, as is the spatially variable monthly mean circulation (Fig. 1b), which varies seasonally (Wilkin 2006; Edson et al. 2007) because of the seasonal variations in wind forcing and inner shelf stratification (Kirincich et al. 2013). The analysis described below uses a residual velocity product, formed by subtracting both the estimated tidal velocities and the monthly mean velocities, from the raw surface current observations. Including tidal velocities in the dataset increased the noise of the eddy detection and tracking due to the spatial variations in tidal phase but led to qualitatively similar results for many of the eddy statistics shown below. However, inclusion of the monthly mean velocities significantly distorted the resulting eddy statistics due to instantaneous realizations of the tidally rectified recirculation present in the northeast corner of the study area.

b. Eddy detection and tracking

This study most closely follows Kim (2010), applying the winding angle method to an estimate of the nondivergent component of the residual velocity field. The two-dimensional nondivergent velocity streamfunction for each time was estimated using a least squares solution to the matrix equation $\mathbf{A}\boldsymbol{\psi} = \mathbf{b}$, where $\mathbf{b}$ is an array of the east u and north v velocities' values at all locations, and $\mathbf{A}$ is a matrix populated by finite-difference approximations for $\boldsymbol{\psi}$ at all locations, as $u = -\partial\boldsymbol{\psi}/\partial y$ and $v = \partial\boldsymbol{\psi}/\partial x$. Tests suggest that the least squares solution for $\boldsymbol{\psi}$ was able to capture the majority of the variance present without resulting in excess variance, or energy, in the recombined flow field. The nondivergent velocity accounted for an average of 67% ± 8% and 52% ± 10% of the total variance for the east and north velocities. Additionally, the sum of the variance predicted by the divergent and nondivergent components was rarely (<5%) greater than 110% of the observed variance. The resulting estimates of $\boldsymbol{\psi}$ were contoured using a constant interval of 25 m^2 s^{-1}, corresponding to a 0.06 m s^{-1} velocity change over the 400-m grid spacing (Fig. 2), shown above to be a conservative estimate of the surface current error. Nearly closed contours that overlap in area were grouped by the direction of velocity rotation to define the grid points of eddylike features.

Use of a constant contour interval ensured that the streamfunction values were comparable across the dataset and that the eddies were above the noise threshold for the radars. Only eddies larger than a minimum size of nine grid points or 1.2 × 1.2 km were saved. The local maximum or minimum of the eddy streamfunction was defined as the eddy center (e.g., Fig. 2). Standard eddy-tracking techniques (e.g., Chelton et al. 2007) were used to link the observed features found in successive times to define each eddy over its lifespan. All eddies lasting longer than 1.5 h were kept for analysis. The propagation distance of each eddy was estimated as the linear distance between the starting and ending locations of the eddy center. The translational speed of the eddy c was estimated from the propagation distance divided by the eddy lifespan, while the rotational speed was defined as the maximum rotational velocity U found within the eddy, averaged over the eddy lifespan following Chelton et al. (2011).

The chosen approach was tested against both the Okubo–Weiss (Chelton et al. 2007) and the vector geometry (Nencioli et al. 2010) approaches of identifying eddies. Inspection of the features detected in each revealed that Okubo–Weiss resulted in higher numbers of false positives, in agreement with previous detailed comparative studies (e.g., Chaigneau et al. 2008; Chelton et al. 2011), while the vector geometry approach underpredicted the eddies present, due in part to the use of detection parameters. However, both the types of eddies found and the basic distribution of the eddy statistics reported (i.e., Fig. 3) were qualitatively similar for all methods.

c. Vorticity equation

The depth-averaged vorticity equation is used here as a diagnostic to assess the role of bathymetry, wind, and bottom friction in driving eddy generation. Assuming constant density and shallow water, following Signell and Geyer (1991),

$$\frac{D\omega}{Dt} = \frac{\omega + f}{H}\left(\frac{DH}{Dt}\right) + \left[\nabla \times \left(\frac{\boldsymbol{\tau}_w/\rho - C_d|\mathbf{u}|\mathbf{u}}{H}\right)\right] \cdot \mathbf{k}, \quad (1)$$

where D/Dt is the material derivative, ω and f are the relative and planetary vorticities, H is the water depth, $\boldsymbol{\tau}_w$ is the wind stress, ρ is the density, C_d is the quadratic bottom drag coefficient, $\mathbf{u}$ is the depth-averaged velocity vector, and $\mathbf{k}$ is the vertical unit vector. The first term on the right side of (1) represents stretching, while the second term describes the source or sink due to the wind and bottom stresses. Expanding the bottom stress term, assuming a constant C_d,

$$-\nabla \times \left(\frac{C_d|\mathbf{u}|\mathbf{u}}{H}\right) = -\frac{C_d|\mathbf{u}|}{H^2} \times \nabla H + \frac{C_d|\mathbf{u}| \times \nabla|\mathbf{u}|}{H} - \frac{C_d|\mathbf{u}|\omega}{H}. \quad (2)$$

The quantities on the right side of (2) describe the effects of slope torque, speed torque, and frictional dissipation

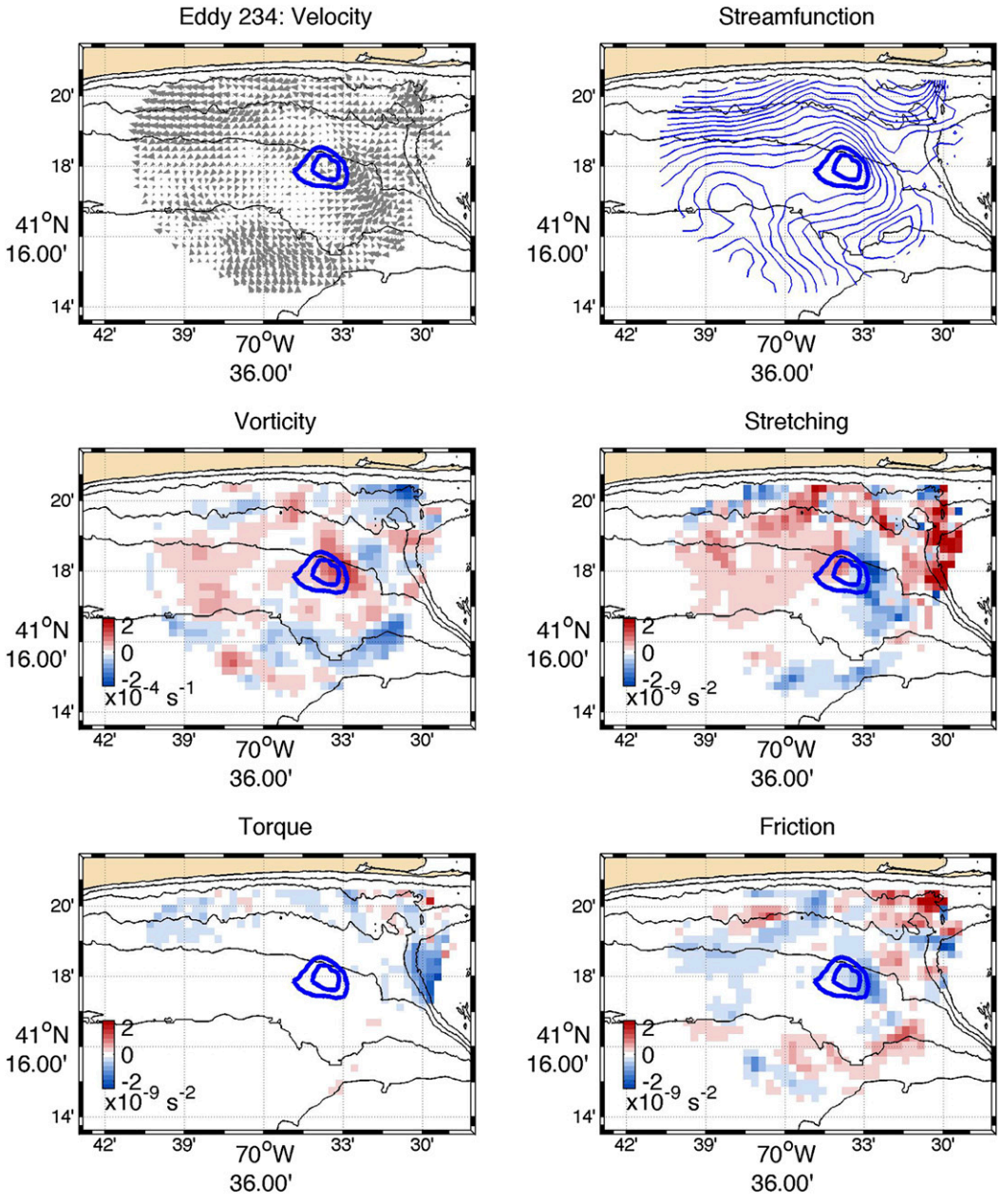

FIG. 2. Example of eddy detection using the nondivergent streamfunction and winding angle method from eddy 234, observed at 0700:00 UTC 14 Jun 2011, along with the vorticity, and the stretching, torque, and frictional components of the vorticity equation. In all panels, the streamlines of the eddy are denoted as the thick, blue contours.

on the creation of vorticity (Signell and Geyer 1991). In general, both the wind and slope torque terms represent sources of vorticity, while the speed torque and frictional dissipation terms represent sinks of vorticity. As neither stratification nor bottom pressure observations were available during the study period, the effects of barotropic and baroclinic pressure gradients (e.g., Huthnance 1984; Cane et al. 1998) are neglected here.

As formulated, (1) and (2) are useful only in determining the role of bathymetry or boundary stresses in generating vorticity that might lead to an eddy. Assuming the surface velocities are representative of the depth-averaged velocities [most likely true inshore of the 20-m isobath (Kirincich et al. 2013)], $C_d = 1.5 \times 10^{-3}$ (Lentz 2001) and spatially uniform winds; time series of the stretching, wind torque, slope torque, speed torque, and

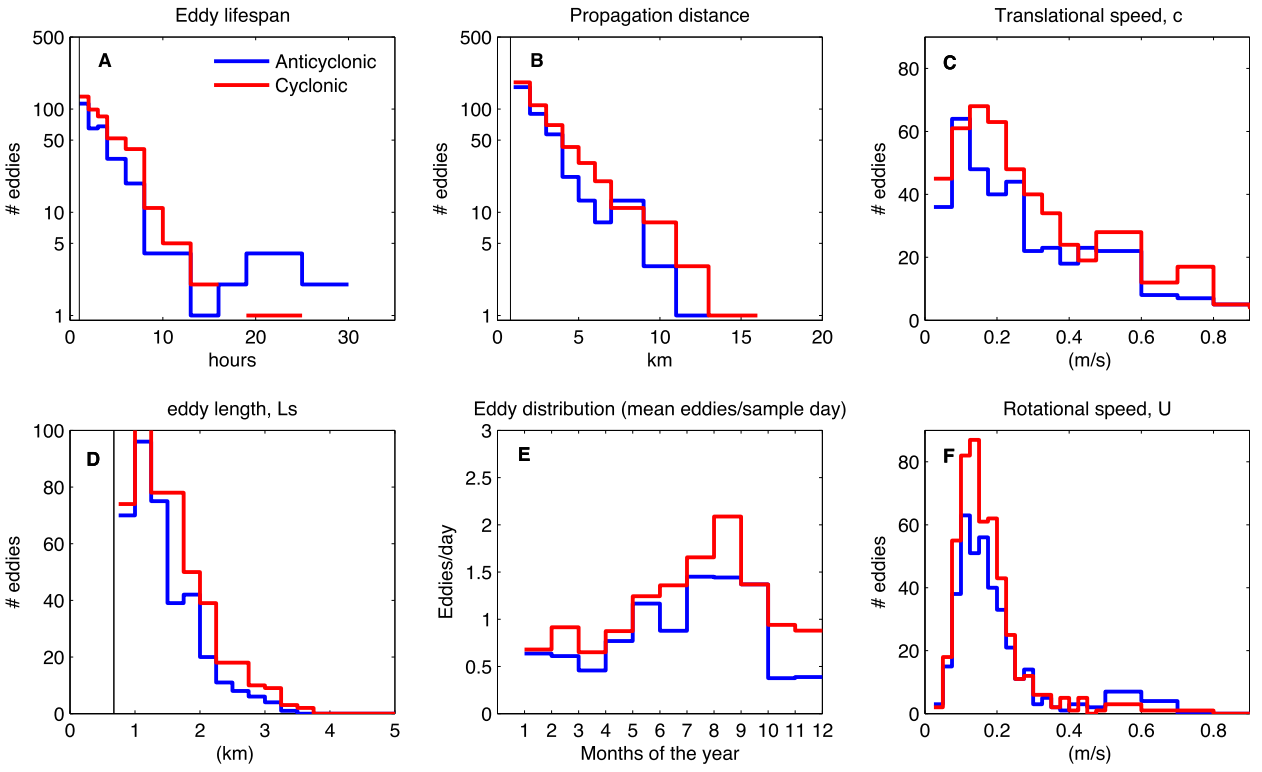

FIG. 3. General statistics for cyclonic (red) and anticyclonic (blue) eddies identified during the study period, including (a) lifespan, (b) propagation distance, (c) translational speed, (d) length scale Ls, (e) seasonal distribution, and (f) rotational speed. The seasonal distribution was estimated by normalizing the number of eddies observed in each calendar month by the number of days sampled in that month.

frictional drag were estimated at each grid point using the observed velocity and vorticity fields. Given a conservative velocity uncertainty of 0.06 m s^{-1}, these terms all have potential errors less than 0.25×10^{-9} s^{-2}. In contrast, uncertainties for $D\omega/Dt$ are much larger, at 1×10^{-7} s^{-2}, and thus the material derivative of vorticity is not included in the analysis. To be concise, the analysis below compares the effects of stretching to the effects of torque (the sum of slope torque and wind torque) and friction (the speed torque and frictional dissipation), as shown in Fig. 2.

d. *Particle tracking*

To estimate the ability of the observed eddies—defined solely by their streamfunction—to trap and move water parcels, a particle-tracking analysis was performed on the surface current observations using the HFR_Progs MATLAB toolbox, which follows Kaplan and Largier (2006). For each eddy, grid points inside the initial location of the eddy were seeded with pseudoparticles and advected for the life of the eddy or until they left the observed domain. These results of particle movement and separation were referenced to a Monte Carlo simulation of the mean separation of a disc of particles, having the same area as the average eddy, seeded at random locations within the middle 50% of the domain, to avoid boundary complications, and at random times when eddies were not present. For each simulation, the mean separation was estimated as the average change in separation between all the seeded particles, having initial separations ranging from 400 m to 2.5 km. Composed of 1000 simulations lasting 8 h, this background separation increases approximately linearly with time to 100 m at 8 h and is an estimate of the diffusion rate of surface currents due to both resolved current structures and the observational errors of the radar system. The relative path of particles within the eddies were also compared to the movement of an along-shelf line of particles, passing through the initial location of the eddy but extending across the study domain, that were advected over the lifespan of the eddy.

3. Results

a. *Statistics*

During the 18-month study period, 866 eddies larger than 1.44 km^2 in area and longer than 1.5 h in lifespan were found within the study area. Detected eddies were somewhat more likely to be cyclonic in rotation; however,

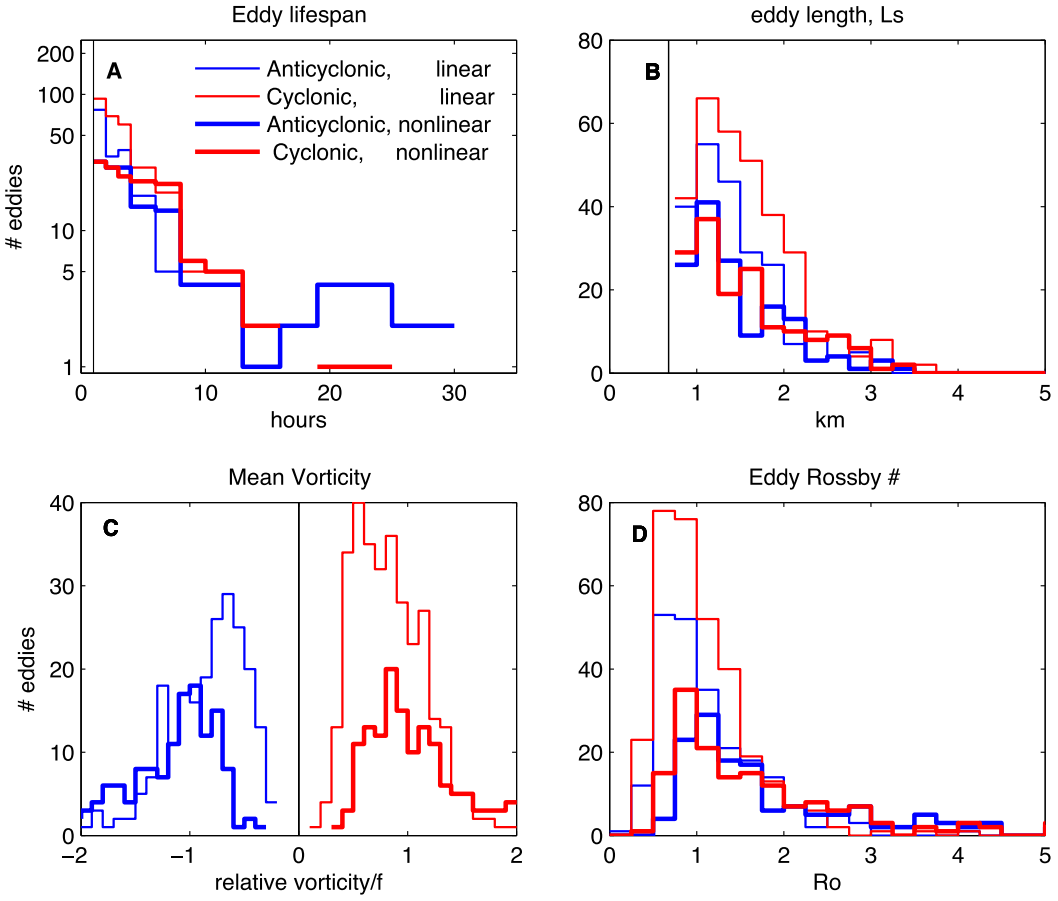

FIG. 4. Statistics of (a) lifespan, (b) length scale Ls, (c) mean vorticity, and (d) eddy Rossby number for cyclonic (red) and anticyclonic (blue) eddies with linear eddies ($U/c < 1$) shown with thin lines and nonlinear eddies ($U/c > 1$) shown with lines.

histograms of eddy lifespan, propagation distance, and size or length scale have similar distributions for cyclonic and anticyclonic eddies (Fig. 3). The logarithm of the number of eddies observed with progressively longer lifespans decreases linearly up to 12 h (Fig. 3a), with only a few eddies lasting longer than 12 h. The distribution of propagation distances had similar shape for cyclonic eddies with a nearly linear decrease from distances of 800 m to 13 km, while propagation distances for anticyclonic eddies decreased more rapidly except for a local maximum of eddies moving 7–8 km (Fig. 3b). Distributions for eddy length scale Ls (Fig. 3d), defined as the radius of a circle having the same area as the mean surface area of the eddy, were similar for both eddy rotations with a peak in the distribution at 1.25 km, corresponding to an area of 5 km^2. The numbers of eddies with length scales greater than this peak decreases rapidly with increasing Ls, with none greater than 4 km detected. Eddy occurrences appear to have a strong seasonal cycle, increasing from 0.5 to 1 day^{-1} in December or January to 1.5 to 2 day^{-1} in August (Fig. 3e). Distributions of translational speed (Fig. 3c) had clear peak values at 0.1 and 0.15 $m\,s^{-1}$ for cyclonic and anticyclonic eddies, respectively, slowly tapering in eddy numbers with increasing speeds up to speeds of 1 $m\,s^{-1}$. In contrast, distributions of rotational speeds (Fig. 3f) peaked much more sharply near 0.15 $m\,s^{-1}$ for both cyclonic and anticyclonic eddies and dropped rapidly in eddy numbers with increasing speeds.

The larger magnitudes found for translational versus rotational speeds implies that, for a fraction of both rotational types, eddies are moving faster than they are rotating. The nondimensional ratio of these speeds U/c has been shown to represent the degree of nonlinearity of rotating vortices (Chelton et al. 2011). Eddies having $U/c > 1$ are more likely to trap fluid within the eddy interior as they translate. Separating the cyclonic and nticyclonic eddies using U/c, linear eddies (i.e., $U/c < 1$) have shorter lifespans and sizes, accounting for the bulk of the eddies shorter than 3 h and the strong peak in eddy lengths between 1 and 2 km (Figs. 4a,b). In contrast, nonlinear eddies (i.e., $U/c > 1$) are on average longer lived and larger in size (Figs. 4a,b).

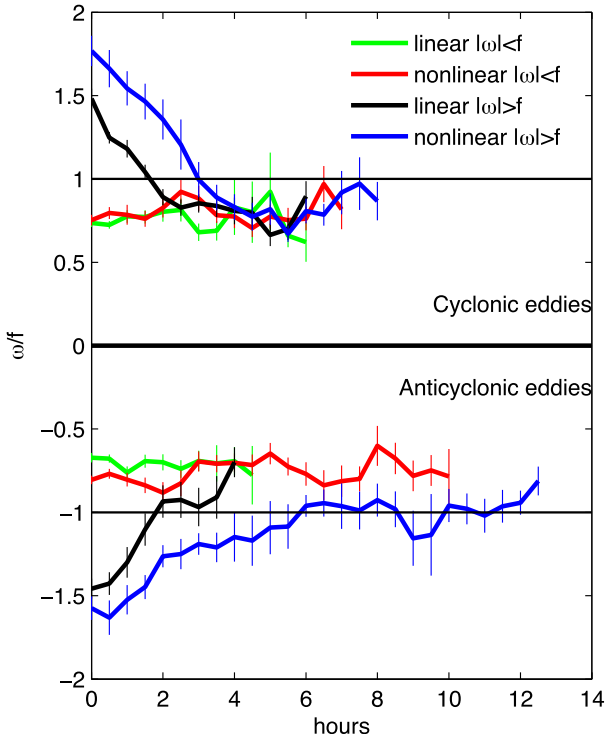

FIG. 5. Average change in relative vorticity, as ω/f, with standard error bounds, over the life of the eddy for both linear ($U/c < 1$) and nonlinear ($U/c > 1$) cyclonic and anticyclonic eddies starting greater and less than $|\omega| = f$. Results are shown for times when 10 or more eddies were present.

Distributions of the eddy-averaged vorticity and estimated Rossby number also show distinct differences based on U/c. Linear cyclonic eddies have a broad distribution of relative vorticity between $0.5f < \omega < f$ (Fig. 4), while nonlinear eddies are shifted to higher values with a broad tail out to $\omega = 2f$. Linear anticyclonic eddies have a narrow peak at $0.7f$ before rolling off at higher values, while nonlinear anticyclonic eddies peak at $-f$. Nearly all observed eddies had Rossby numbers, estimated as $\mathrm{Ro} = U/f\mathrm{Ls}$, greater than 0.5, suggesting that nonlinear advection is important to most of the eddies found. Linear eddies had a strong peak at $\mathrm{Ro} = 1$ and a rapid fall off to 2. Nonlinear eddies had a smaller peak at $\mathrm{Ro} = 1$ and a long tail out to values as high as 4.5 with similar distributions for both rotational directions.

A significant fraction of the eddy-averaged vorticity for eddies of both rotational directions was greater in magnitude than $|\omega| = f$ (Fig. 4). These elevated levels of mean vorticity were caused by eddies that evolved rapidly in time. On average, the relative vorticity of cyclonic eddies starting with $\omega > f$ decreased rapidly to $0.8f$ within 2–3 h, matching the mean relative vorticity of eddies starting $<f$ (Fig. 5). Linear anticyclonic eddies with initial relative vorticities less than $-f$ start at an average vorticity of $-1.5f$ before quickly decreasing to $-f$ at 2 h and $-0.8f$ by 4 h (Fig. 5). However, the relative vorticity of nonlinear anticyclonic eddies starting less than $-f$ decreased more slowly, stabilizing at $-f$ over a 6-h period. Eddies starting with relative vorticity less than f remained at similar values throughout their lifespan (Fig. 5), independent of U/c.

Eddies were most prevalent along the eastern side of the study area, with the density of eddies varying seasonally for both rotational directions (Fig. 6). During winter when stratification is weaker (Lentz et al. 2008), defined here as November to April, the spatial peak in eddy density is located at 41°18′N and 70°31′W, just west of Wasque Shoal for both rotation directions (Figs. 6b,e). Eddies not adjacent to the eastern edge of the study area during winter, primarily cyclonic eddies east of 70°33′W, were due west of the peak. When conditions are more likely to be stratified during summer months (Lentz et al. 2008), defined here as June to September, the area of anticyclonic eddies (Fig. 6c) spreads from the eastern edge both offshore along the southeastern edge of the study area and to the northwest in larger numbers. Cyclonic eddies were even more widely distributed than anticyclonic eddies in summer months (Fig. 6f).

b. Drivers

Winds measured at MVCO's offshore tower were predominately toward the northeast during summer but stronger and more variable in direction during winter (Fig. 6). As winds are generally onshore, it is possible that eddies are generated via an interaction of the wind-driven currents and the variable along-shelf bathymetry (Fig. 1). To understand if wind direction played a role in eddy generation, the distribution of wind direction present during the first half of each eddy's lifespan, during summer only because of the larger spatial distributions present, was compared to the overall directional distribution of wind (Table 1). Only a few combinations of eddy and wind directions occurred more often than the distributions of the winds themselves, including linear eddies during winds toward the northeast and nonlinear anticyclonic eddies during winds to the northwest (Table 1), suggesting that wind direction played a role in the formation of these types of eddies. For all other combinations of eddies and wind quadrants, the distributions of wind directions during eddies were not significantly different than wind distributions for all times.

While the wind direction is associated with the formation of some eddies, wind direction was also linked to where the eddies were found within the study area. Examining the relative location of eddy centers and tracks during winds toward the northeast (NE) and

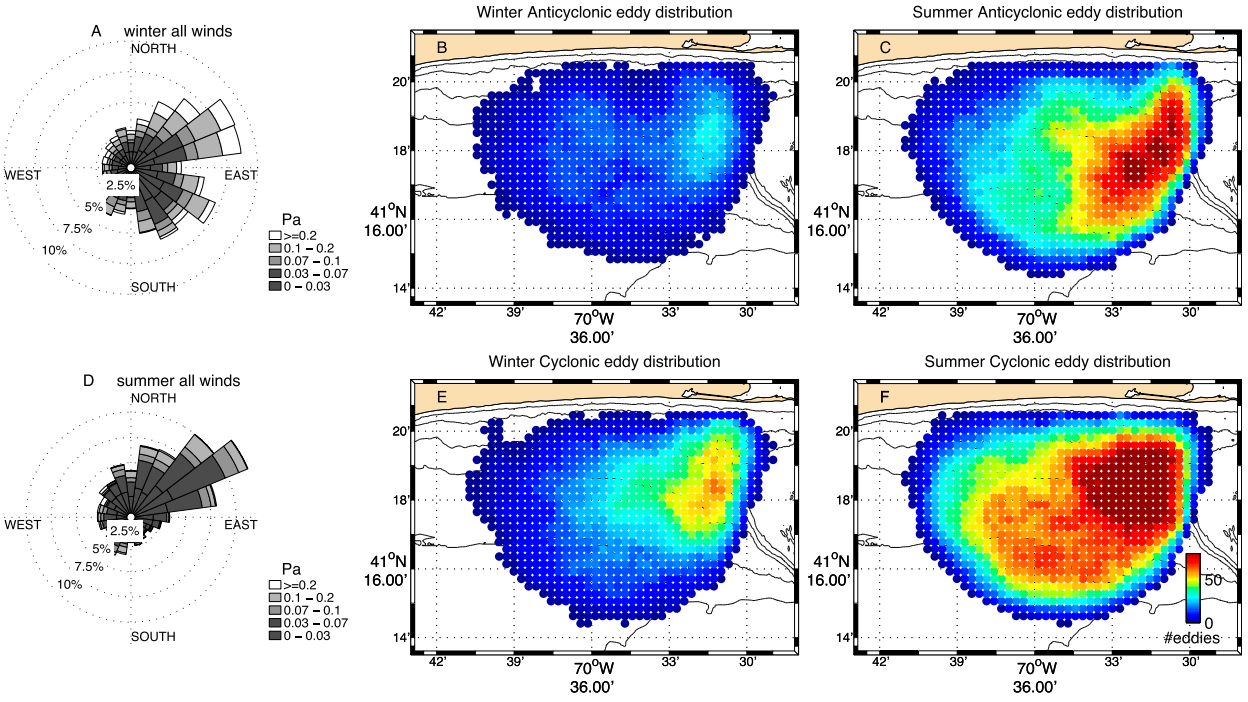

FIG. 6. (a) Winter (November to April) and (d) summer (June to September) wind stress (Pa) histograms along with eddy densities, defined as the total number of eddies seen at a grid point, for (b),(c) anticyclonic and (e),(f) cyclonic eddies in winter and summer, respectively.

northwest (NW) quadrants (Fig. 7), which dominate during summer, anticyclonic eddies were predominantly found on the eastern side during winds to the NW but throughout the domain during winds to the NE. Linear cyclonic eddies were concentrated in the NE corner during winds to the NE, but more evenly distributed for winds to NW (Fig. 7b). In contrast, nonlinear cyclonic eddies were found in the west during NW winds and in the east during NE winds (Fig. 7d).

The role of tides in generating eddies was examined by comparing the observed start of the eddies relative to the phase of the dominant M_2 tide (Fig. 8). This phase was randomly (i.e., more uniformly) distributed for eddies forming outside of the northeast corner of the study area, arbitrarily defined as north of 41°17′N and east of 70°34′W, suggesting no link between the direction of tidal currents and eddy generation. However, cyclonic eddies forming inside the northeast corner had notably larger occurrence rates during the relative phases of −70° to 20° degrees, when the tide changes from slack water to maximum ebb (i.e., tidal velocities flow westward from Wasque Shoal; Fig. 8c). A second area of increase occurrences exists at phases of 70° to 150° for cyclonic eddies (Fig. 8). Anticyclonic eddies forming inside the northeast corner have a slight increase in occurrences for phases 100°–180°.

Cyclonic eddy generation during flow into deeper waters (phases of −70° to 20°; Fig. 8) is consistent with

TABLE 1. Occurrence of eddies (as % of the total distribution) by wind direction quadrant during summer.

	Southwest	Southeast	Northeast	Northwest
	180°–270°T	90°–180°T	0°–90°T	270°–0°T
June–September winds[a,b]	18	13	48	21
Linear				
Cyclonic	8	12	60	20
Anticyclonic	11	15	55	19
Nonlinear				
Cyclonic	16	19	48	18
Anticyclonic	14	11	43	31

[a] As % of the total distribution.
[b] Wind direction is defined using the oceanographic convention or the direction to which the wind blows.

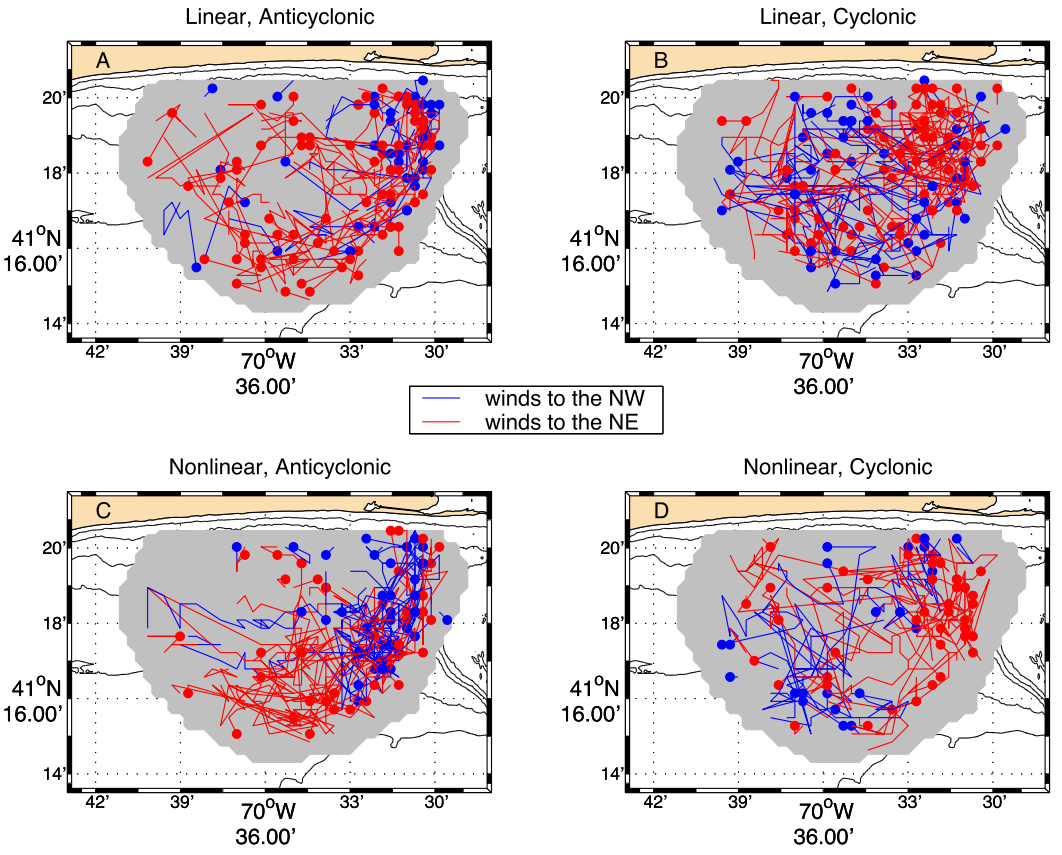

FIG. 7. Starting positions (dot) and tracks (line) of the eddy centers for (a),(c) anticyclonic and (b),(d) cyclonic eddies during summer. Eddies occurring during winds to the NW and NE are shown in blue and red, respectively.

the generation of positive (cyclonic) vorticity via vortex stretching (i.e., Robinson 1981). Similarly, an onshore and upslope tidal flow (phase > 100°; Fig. 8) would generate negative (anticyclonic) vorticity and potentially contribute to anticyclonic eddies. While the change between ebb and flood that occurs between phases of 70° and 150° is not itself conductive to cyclonic vorticity generation, 1) the tide offshore (station B in Fig. 1) has a significant onshore component that is northward during phases of 70°–150° (Fig. 8), and 2) a 50° phase lag exists moving west along the shelf (Fig. 1). Thus, when slack water exists at location C at phase = 75°, the tide is to the west at location A and flowing onshore at location B. The spatial differences in tidal flows among these locations give rise to a cyclonic sense of rotation in the northeast corner. How this might translate into increased eddy generation is not known as, following Robinson (1981), this mechanism must compete with a negative or anticyclonic vortex stretching of the onshore, upslope flow at C.

The potential role of vortex stretching in driving vorticity and eddy generation can be examined by comparing the magnitudes of the stretching, torque, and friction terms in the vorticity equations [(1), (2)], shown in Fig. 9 as eddy averages at the start of each eddy's lifespan. It is important to note that only 61% (25%) of cyclonic (anticyclonic) eddies had eddy-averaged stretching magnitudes above the noise threshold of $0.25 \times 10^{-9}\,\mathrm{s}^{-2}$ and are shown in Fig. 9. Of the measurable cyclonic eddies, vortex stretching acts as a source of vorticity along much of the northern portion of the domain, with these gains in cyclonic vorticity opposed by the frictional terms. However, along the eastern edge and farther offshore, the eddy-averaged stretching term is negative. As a fraction of cyclonic eddies in both phase peaks (Fig. 8) were observed to have negative stretching, these results suggest that vorticity, and thus eddy, generation is likely more complex than tidally driven vortex stretching alone for cyclonic eddies. Wind or slope torque was generally a sink of vorticity for cyclonic eddies and only sizable to the east. In contrast to cyclonic eddies, the majority of the anticyclonic eddies with measurable vorticity terms had negative stretching when first observed, while the torque is generally negative onshore but positive along the eastern edge over Wasque Shoal (Fig. 9). For both eddy

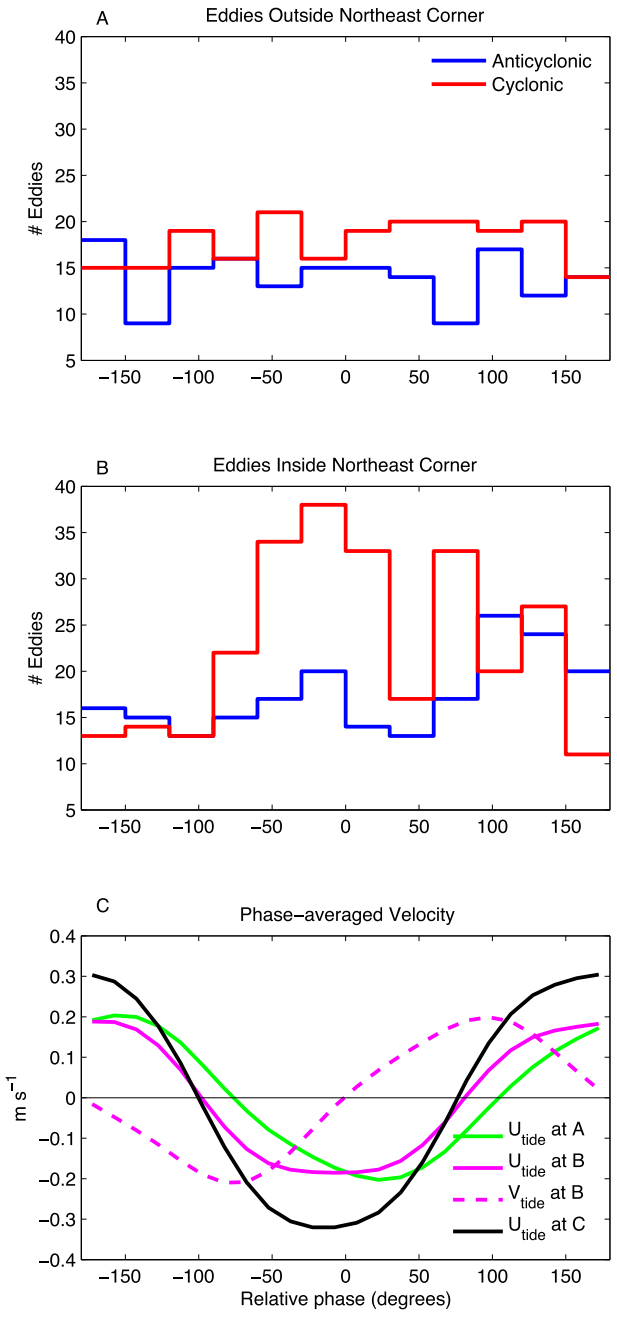

FIG. 8. Histograms of the relative phase at the start of cyclonic and anticyclonic eddies found (a) outside and (b) inside of the northeast corner of the study area, defined as north of 41°17′N and east of 70°34′W, compared to the phase of the dominant M_2 tidal constituent measured at 41°19′ N, 70°32′W. (c) Phase-averaged east and/or north components of the M_2 tide at locations A, B, and C shown in Figs. 1 and 9 (see text for details).

types, the effects of slope and wind torque were usually smaller than the stretching term and/or opposed an increase in vorticity. However, few of the eddies found offshore and to the west had significant stretching or torque terms despite similar levels of vorticity, suggesting a breakdown in the assumptions used to formulate the vorticity equations as applied here.

c. *Secondary circulation*

A more nuanced picture of the surface structure of the types of eddies described above can be made by averaging over multiple eddies, each normalized by its length scale Ls and observed in an eddy-following coordinate frame. Shown in Fig. 10, this type of composite view of eddies starting within the northeast corner illustrates both the relative structure of the eddies and the role of stretching within the eddy. The velocity fields of the eddies (Fig. 10) are not symmetric, as the area of maximum absolute vorticity is offset from the center, defined by the peak of the local streamfunction. Thus, the composite eddies appear to have a weaker northeastern side, where rotational velocities are smaller and the area of maximum vorticity is located, and a stronger west to southwestern side opposite the weak, where the rotational velocities are larger. As a result, surface currents are convergent on the strong side and divergent on the weak side of anticyclonic eddies, with the divergent component of the surface circulation flowing from the weak to strong sides of the eddy. For cyclonic eddies, the pattern is reversed, with divergence on the strong side, convergence on the weak side, and surface flow from the strong to weak side. Vortex stretching (Fig. 10) is generally negative along the weak eastern side of anticyclonic eddies but weak within the rest of the eddy. In contrast, stretching switches sign across cyclonic eddies, from negative (opposing the creation of cyclonic vorticity due to stretching) in the east to positive in the west.

4. Effect on transport and exchange

While it is clear that more can be learned about the drivers and dynamics of the eddies observed south of Martha's Vineyard, a central motivation for this study was to assess their potential contribution on the exchange across the inner part of the shelf. By simple metrics such as the total onshore drift of the eddies or their kinetic energy, their contribution to the flow field was relatively small. The mean translation due to all eddies was approximately 500 m to the southwest. Comparing the eddy kinetic energy (EKE), estimated as $(0.5/N)\sum[(u')^2 + (v')^2]$, where N is the number of samples and the prime denotes velocity perturbations around the spatial mean velocity for each time, for the entire study area to those areas identified as eddy cores, eddies were responsible for <1% of the total EKE in winter (November–March) and 3% in summer (June–September). Even when considering only times

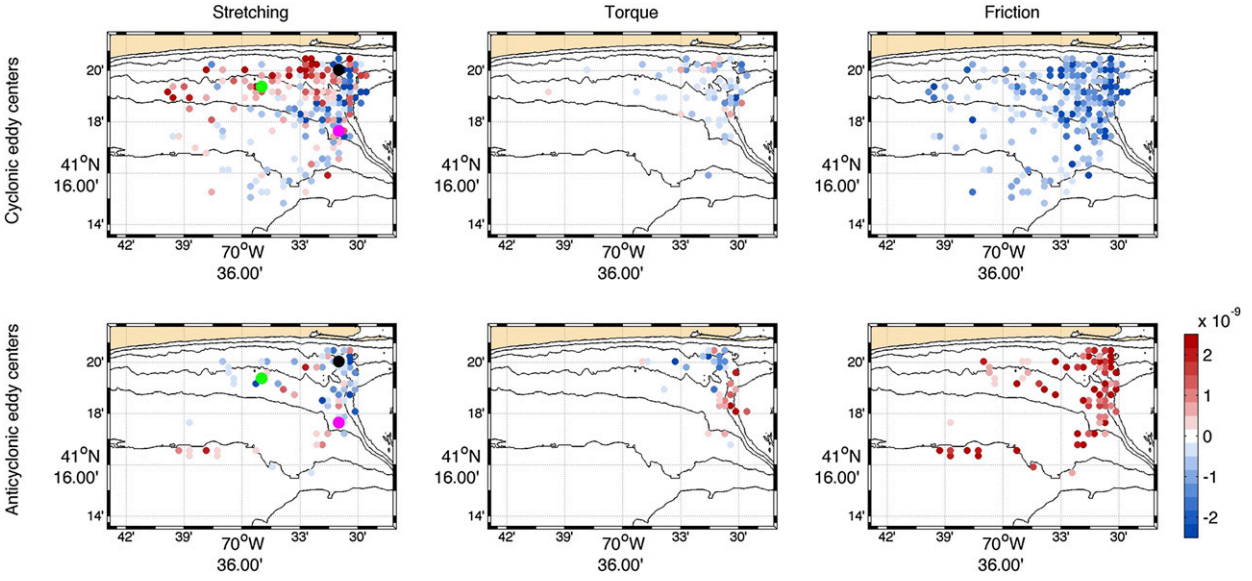

FIG. 9. Spatially averaged (left) stretching, (center) torque, and (right) frictional terms (s^{-2}) from the vorticity equations [(1), (2)] for (top) cyclonic and (bottom) anticyclonic eddies. In each panel, the average value of the term over the area defined as the eddy at the eddy start is shown at the initial location of the eddy center. If multiple eddies shared the same center location, the mean over all eddies is shown. The location of the phase-averaged tidal velocities shown in Fig. 8 is included in the left-hand side panels.

when eddies were present, the ''eddy'' EKE was 13% of the total. However, such metrics are a poor descriptor of the eddy's effect on the movement of water masses across the shelf.

The percent of particles retained within the eddy over its lifespan (Figs. 11a,c), where ''retained'' is defined as being within 400 m of any eddy grid point for that time step, provides an assessment of how well observed eddies trapped or retained potential fluid particles. For linear eddies of both rotations, the percentage of particles remaining within the eddy over its lifespan, or until a particle reaches the boundary, decreased from 100% at inception to 30% and 24% at 4 h for anticyclonic and cyclonic, respectively. For nonlinear eddies, the retention rate increased, with more than 40% of particles retained for up to 6 h on average.

The retentiveness of the eddies observed is important only if it is significantly different than the background separation of the flow field. For cyclonic eddies, separations are less than background levels (Figs. 11b,d) until hour 4 when the results increase to background separation rates or become more variable. Anticyclonic trajectories are more convergent on average with negative separations for all but the last hour of significant results for nonlinear eddies. Thus, for most eddies the separation rates are significantly less than background levels, meaning the eddies are more retentive than the background flow, until a transition point is reached and rates increase to background levels. For all but linear anticyclonic eddies, the transition point occurs after a majority of the particles have left the eddy (Fig. 11), suggesting that the change in particle composition (inside versus outside) leads to the increase.

While more retentive than the background diffusion present, a key result of the particle trajectory analysis is that eddies in the study area are partially leaky. Coupling this leakiness with the fact that eddy length scales were generally larger than translational distance and that eddies were short lived (Figs. 3a,b,c), the role of an eddy's rotational velocity component in moving water parcels from one side of the eddy to another over the eddy's lifetime, that is, the eddy's ''rotational effect,'' has the potential to dominate the eddy's total effect on individual water parcels. The lateral exchange of particles over the lifespan of the eddy can be estimated from the particle-tracking results, assuming each is representative of a volume of water equivalent to a grid point with area 400 m $\times$ 400 m and a uniform 5-m thick mixed layer depth. Typical for the region (Fewings et al. 2008), the 5-m mixed layer depth was assumed only to estimate results as a volume flux per unit along-shelf distance. The mean across-shelf displacement of all particles starting within the eddy is representative of the mean translation of the eddy and therefore a mean flux of volume across an arbitrarily defined along-shelf plane. However, the rotational effect exists in addition to this mean translation and can be estimated via the sum of the displacement of all parcels that move farther across shore than the mean translation, differenced from the mean translation. All results were normalized by the

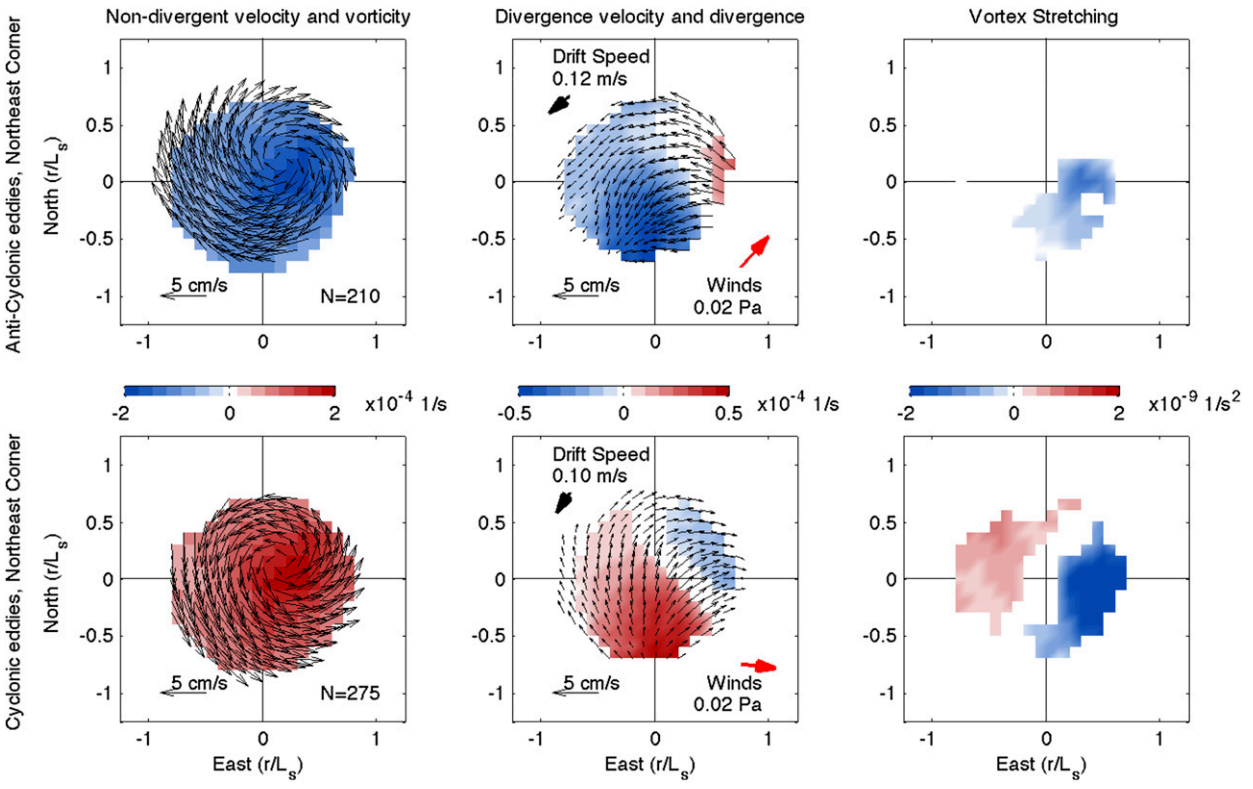

FIG. 10. Normalized (left) vorticity and residual velocities, (center) divergence and divergent velocity, and (right) vortex stretching for all (top) anticyclonic and (bottom) cyclonic eddies starting in the northeast corner, that is, east of 70°34′W and north of 41°17′N. Results are shown where the magnitude of the conditionally averaged quantity was greater than its standard error. Based on error analysis, surface divergences less than $0.1 \times 10^{-4}\,s^{-1}$ (equal to $0.86\,m\,day^{-1}$ of upwelling) are below the noise level for the radar observations and not shown. The mean eddy drift and wind speed and directions are shown in the center panels.

20-km, nominal, along-shelf extent of the study area to place the results in units of meters squared per second, or volume transport (meters cubed per second) per meter in the along-shelf direction, and be directly comparable to more typical estimates of wind-driven transport (e.g., Huyer 1983).

In winter, eddies cause net offshore transport due to translation and a similar magnitude of relative exchange due to their rotational effect (Table 2). In summer, linear cyclonic eddies had the largest impact with 4.5 and $3.5 \times 10^4\,m^2\,s^{-1}$ of translational and relative exchanges. Despite their larger sizes, the exchange by nonlinear eddies was significantly less ($<1 \times 10^4\,m^2\,s^{-1}$) than linear eddies because of their reduced occurrence rates. In both summer and winter the translational exchange across the along-shelf line was near zero, which suggests that the along-shelf scales of lateral variability were smaller than the domain examined. The rotational exchange across the along-shelf line was only slightly more than the eddy relative exchange, suggesting that the core of the eddies themselves accounted for more than half of the lateral exchange present.

The aggregate of both the translational and relative effects for all summer eddies gives an estimated across-shelf exchange of $15.6 \times 10^4\,m^2\,s^{-1}$. Importantly, relative exchange contributed as much or more than translational exchange. For comparison, an estimate of the wind-driven across-shelf exchange over the same period, based on observed winds as $U_{ek} = a\tau_w^y/\rho f$, where $a = 0.25$ accounts for the reduced Ekman transport present in shallow, inner-shelf waters (Lentz 2001; Kirincich et al. 2005), was $-27.7 \times 10^4\,m^2\,s^{-1}$, directed offshore. Thus, given the assumptions used here, the eddy field observed has the potential to cause significant amounts of across-shelf exchange relative to the wind-forced, depth-dependent exchange. However, more work is needed to fully account for both the vertical structure of eddies over the inner shelf as well as how efficiently they are able to transport or exchange water properties.

5. Discussion

The small size and short lifespans of the eddies found here are significantly different from open-ocean

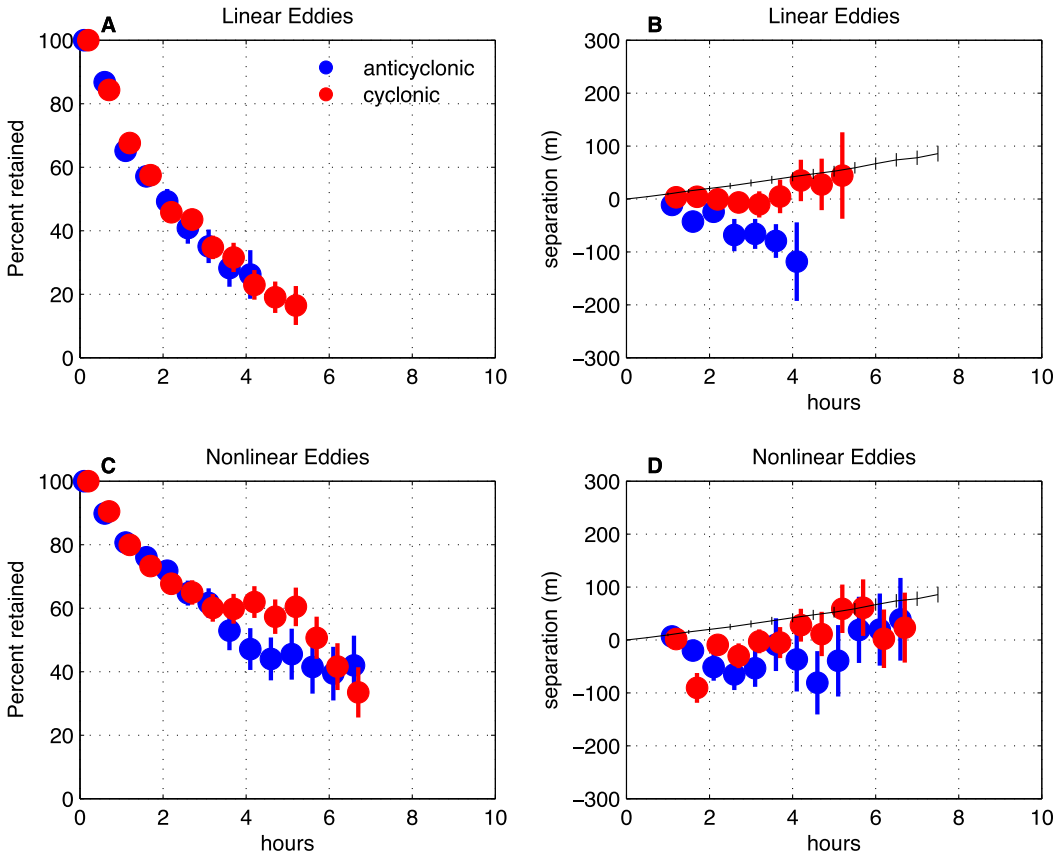

FIG. 11. (a),(c) Mean percent of pseudoparticles remaining within the eddy over the lifetime of the eddy for linear and nonlinear eddies. (b),(d) Mean change in separation between pseudoparticles launched within the eddy at inception for linear and nonlinear eddies, compared to an estimate of the background separation, or diffusion, of the surface current observations (thin black line with standard error bounds, see text for details). For both calculations, the number of eddies in each sample was greater than 20.

mesoscale eddies (e.g., Chelton et al. 2011) as well as the coastal mesoscale or submesoscale features previously described using HF radar (e.g., Nencioli et al. 2010; Kim 2010). Despite high Rossby numbers, they are also decidedly weaker than the headland eddies modeled by Signell and Geyer (1991), who suggested that eddy vorticity near bathymetric features comparable to Wasque Shoal could be up to $10f$ and have clear phase locking of the vortex generation and separation mechanisms. Most observed eddies here were less than 5 h in duration, smaller than 4 km in diameter, and rotated less than once over their lifespan. Linear eddies ($U/c < 1$) were shorter, smaller, and generally weaker in strength in comparison to nonlinear eddies ($U/c > 1$). As suggested by Chelton et al. (2011), nonlinear eddies were more likely to trap fluid and advect a core of fluid. However, as linear eddies occurred more often than nonlinear eddies, both their translational and rotational effects dominated the overall contribution of eddies to lateral exchange across the inner shelf.

Observed eddies were responsive to the wind direction, in that variations in wind forcing offered some predictive capacity for when and where eddies were likely to form. Despite this, the exact mechanism of vortex generation, that is, flow separation of the wind-driven coastal current around Wasque Shoal, was not discernible with the observations at hand. For example, if the wind is toward the NW during summer, it is likely that either an anticyclonic eddy will form along the east side of the domain or a cyclonic eddy will form on the west side. During winds to the NE, cyclonic eddies generally form inshore in the east. With combined eddy occurrence rates of 1 day^{-1} in winter and up to 4 day^{-1} in summer, most wind ''events'' are likely to have an eddy associated with them. While local bathymetry clearly played an important role in generating eddies, as most were found along the eastern boundary, a smaller number (~¼) of the observed eddies were directly linked to the phase of the M_2 tide within the northeast corner and consistent with vortex stretching

TABLE 2. Mean across-shelf exchange ($\times 10^4\,m^2\,s^{-1}$), integrated over all eddies.

	Summer				Winter			
	Eddy core		Along-shelf line		Eddy core		Along-shelf line	
Eddy type	Translational	Rotational	Translational	Rotational	Translational	Rotational	Translational	Rotational
Linear								
Anticyclonic	2.35	2.30	0.01	3.67	−1.70	1.32	−0.00	1.63
Cyclonic	4.57	3.51	0.01	7.54	−1.60	1.44	−0.00	1.85
Nonlinear								
Anticyclonic	0.65	0.58	−0.00	1.18	−1.75	1.29	−0.00	1.60
Cyclonic	0.78	0.82	−0.00	1.58	−0.57	0.88	−0.00	1.16

of the tidal flow. As the interaction of the wind-driven flow with the shoal appears to be the overarching cause of eddy generation, inner shelf areas with bathymetric features are likely to see similar levels of increased lateral stirring at a range of scales in the areas adjacent to the feature, independent of the role of tides.

In the study area, the observed eddies had a sizable contribution to the amount of volume exchanged across the shelf relative to the estimated wind-driven transport, with important implications. Kirincich et al. (2013) showed that the surface heat budget south of Martha's Vineyard was significantly impacted by cooling due to an advective heat flux with both a mean and time-varying or eddy component. The effect of the eddy component was the opposite of the onshore transport predicted by local wind-driven upwelling/downwelling (Kirincich et al. 2013) and could be accounted for by the actual eddies found here both because of their translational effect and the rotational stirring of the mean gradient of sea surface temperature (Kirincich et al. 2013). However, detailed estimates of the vertical scale of the eddies are critical to further constrain the magnitude of their effect on exchange.

Finally, a number of aspects of the observed eddies require further discussion. The patterns of surface divergence and asymmetric vorticity in the composite eddies (Fig. 10) are notable in that they are not typically seen in oceanic eddies. A wind-driven secondary circulation similar to that seen in oceanic mesoscale eddies (McGillicuddy et al. 2007; Mahadevan et al. 2008) for a cyclonic eddy would result in either axisymmetric divergence, for a linear Ekman forced effect, or a symmetric pattern across the axis of the wind direction, for a nonlinear effect. Both effects are inconsistent with the patterns of divergence observed here (Fig. 10), potentially because of the large Rossby numbers and small scales seen here. The signature of a propagating sea level anomaly observed via surface velocities is more likely at these scales and matches the pattern of divergences shown for both eddy types. For instance, the translating sea level maxima associated with an anticyclonic eddy could appear as a convergence at the leading edge and a divergence at the trailing edge, with divergent velocities toward the leading edge. However, the alignment of the divergence pattern with the mean direction of eddy drift (Fig. 10) is not found with all eddy types and, when present, appears to be only by chance. Thus, this analysis suggests that the observed eddies are strongly affected by the wider area circulation, which acts to distort the symmetry of the eddy and leading to the pattern of divergence found. True for both types shown in Fig. 10 as well as eddies found offshore, the ''strong'' side of the eddy is adjacent to either the core of the coastal current for anticyclonic eddies or the stronger presumably wind-driven velocities of the wider area circulation for the cyclonic eddies.

A more detailed examination of the vorticity balance [(1), (2)] during eddy generation and decay was not possible because of the limitations of the observations. While stretching was the dominant vorticity component shown in Fig. 9, only 61% (25%) of cyclonic (anticyclonic) eddies had eddy-averaged stretching magnitudes above the noise threshold of $0.25 \times 10^{-9}\,s^{-2}$. With few of the eddies found offshore and to the west having measurable stretching, combined with the fact that offshore-forming eddies were generally large in size relative to the scale of the sloping bottom, it is likely that these eddies were confined to the surface layer. Thus, baroclinic processes, ignored here for lack of observations, were likely important in creating vorticity and therefore eddies offshore.

Further, along the shallow eastern boundary where eddies are most likely to span the water column and the depth-averaged vorticity equation is likely a reasonable approximation, the sum of the eddy-averaged stretching, torque, and frictional components were often as large as the stretching term, suggesting that the advection of vorticity might also be important. It is also apparent from Fig. 5 that, apart from the initial decreases of eddies starting above $|f|$ due in part to known instabilities (e.g., Rudnick 2001; Shcherbina et al. 2013), vorticity does not generally decrease toward the end of

the eddy. Vorticity magnitudes in the area of the eddy are as high immediately following the eddy as they are during the eddy (not shown here). Thus, vorticity itself is not a clear indicator of the strength and/or decay of an eddy. While this is potentially an artifact of the eddy detection method chosen, as the winding angle method is based on the velocity streamfunction, it might also suggest that eddy features might transition into ''squirts'' or ''jets'' not having a closed contour without a measurable change in vorticity. Regardless, a more detailed examination of the dynamics of these types of coherent features over the inner shelf, despite their generation by processes as simplistic as tidally driven vortex stretching, requires detailed stratification and bottom pressure observations along with the type of high-resolution currents used here.

6. Summary

High-resolution observations of surface currents in the inner shelf south of Martha's Vineyard, Massachusetts, were used to investigate the statistics of small $O(2–5)$ km, submesoscale eddies, and their implications for lateral exchange. Within the 300 km^2 study area, eddies occurred at rates of 1 to 4 day^{-1}, with the seasonality driven by the occurrence of significantly more eddies offshore during summer. Most eddies were less than 5 h in duration, smaller than 4 km in diameter, and rotated less than once over their lifespan. Despite the proximity to Wasque Shoal, few of the eddies found had a clear connection to ''tidal'' forcing that would result in phase locking of the eddies to the M_2 tide. Instead, the majority of features present appeared randomly distributed in phase, yet dependent on the direction of the wind forcing and the existence and location of an along-shelf coastal current during summer. The nonlinear parameter U/c linked key differences in the kinematics of the eddies, including the lifespan, vorticity, and Rossby number. Seeding the Eulerian flow field with pseudoparticles, eddies were found to be more retentive than the background flow field but still leaky, particularly for linear eddies ($U/c < 1$). Eddies closer to Wasque Shoal, east of 70°33′W, move west on average, while eddies farther west have minimal translations but cause potentially significant amounts of relative exchange. The estimates of transport and exchange due to eddies, assuming a constant vertical scale, suggest that both the eddies and the flow fields that create them play an important role in the total across-shelf exchange of volume present between the nearshore and the larger coastal ocean offshore.

Acknowledgments. The HF radar data utilized here were obtained using internal funding from the Woods Hole Oceanographic Institution. The analysis was supported by NSF OCE Grant 1332646. The author thanks Steve Lentz, Irina Rypina, Ken Brink, and Rocky Geyer for their helpful comments and insight. Additionally, the comments of two anonymous reviewers greatly improved the substance and the presentation of the manuscript. (The raw data used in this study are available at http://hdl.handle.net/1912/8018.)

REFERENCES

Austin, J. A., and S. J. Lentz, 2002: The inner shelf response to wind-driven upwelling and downwelling. *J. Phys. Oceanogr.*, **32**, 2171, doi:10.1175/1520-0485(2002)032<2171:TISRTW>2.0.CO;2.

Barth, J. A., S. D. Pierce, and R. M. Castelao, 2005: Time-dependent, wind-driven flow over a shallow midshelf submarine bank. *J. Geophys. Res.*, **110**, C10S05, doi:10.1029/2004JC002761.

Beckenbach, E., and L. Washburn, 2004: Low-frequency waves in the Santa Barbara Channel observed by high-frequency radar. *J. Geophys. Res.*, **109**, C02010, doi:10.1029/2003JC001999.

Cane, M., V. Kamenkovich, and A. Krupitsky, 1998: On the utility and disutility of JEBAR. *J. Phys. Oceanogr.*, **28**, 519–526, doi:10.1175/1520-0485(1998)028<0519:OTUADO>2.0.CO;2.

Capet, X., J. McWilliams, M. J. Molemaker, and A. F. Shchepetkin, 2008: Mesoscale to submesoscale transition in the California Current System. Part III: Energy balance and flux. *J. Phys. Oceanogr.*, **38**, 2256–2269, doi:10.1175/2008JPO3810.1.

Castelao, R. M., and J. A. Barth, 2006: The relative importance of wind strength and along-shelf bathymetric variations on the separation of a coastal upwelling jet. *J. Phys. Oceanogr.*, **36**, 412–425, doi:10.1175/JPO2867.1.

Chaigneau, A., A. Gizolme, and C. Grados, 2008: Mesoscale eddies off Peru in altimeter records: Identification algorithms and eddy spatio-temporal patterns. *Prog. Oceanogr.*, **79**, 106–119, doi:10.1016/j.pocean.2008.10.013.

Chant, R. J., 2004: Flow reversals during upwelling conditions on the New Jersey inner shelf. *J. Geophys. Res.*, **109**, C12S03, doi:10.1029/2003JC001941.

Chapman, R. D., L. K. Shay, H. C. Graber, J. B. Edson, A. Karachintsev, C. L. Trump, and D. B. Ross, 1997: On the accuracy of HF radar surface current measurements: Intercomparisons with ship-based sensors. *J. Geophys. Res.*, **102**, 18 737–18 748, doi:10.1029/97JC00049.

Checkley, D. M., and J. A. Barth, 2009: Patterns and processes in the California Current System. *Prog. Oceanogr.*, **83**, 49–64, doi:10.1016/j.pocean.2009.07.028.

Chelton, D. B., M. G. Schlax, R. M. Samelson, and R. A. de Szoeke, 2007: Global observations of large oceanic eddies. *Geophys. Res. Lett.*, **34**, L15606, doi:10.1029/2007GL030812.

——, ——, and ——, 2011: Global observations of nonlinear mesoscale eddies. *Prog. Oceanogr.*, **91**, 167–216, doi:10.1016/j.pocean.2011.01.002.

de Paolo, T., E. Terrill, and A. Kirincich, 2015: Improving SeaSonde radial velocity accuracy and variance using radial metrics. *Proc. OCEANS 2015*, Genoa, Italy, IEEE, doi:10.1109/OCEANS-Genova.2015.7271360.

Edson, J. B., and Coauthors, 2007: The Coupled Boundary Layers and Air–Sea Transfer experiment in low winds. *Bull. Amer. Meteor. Soc.*, **88**, 341–356, doi:10.1175/BAMS-88-3-341.

Fewings, M., S. J. Lentz, and J. Fredericks, 2008: Observations of cross-shelf flow driven by cross-shelf winds on the inner

continental shelf. *J. Phys. Oceanogr.*, **38**, 2358–2378, doi:10.1175/2008JPO3990.1.

Ganju, N. K., S. J. Lentz, A. R. Kirincich, and J. T. Farrar, 2011: Complex mean circulation over the inner-shelf south of Martha's Vineyard revealed by observations and a high-resolution model. *J. Geophys. Res.*, **116**, C10036, doi:10.1029/2011JC007035.

Geyer, R., and R. Signell, 1990: Measurements of tidal flow around a headland with a shipboard acoustic Doppler current profiler. *J. Geophys. Res.*, **95**, 3189–3197, doi:10.1029/JC095iC03p03189.

Halle, C., 2008: HF radar processing using nearest-neighbor statistics. Bodega Marine Laboratory Tech. Rep., 26 pp.

Huthnance, J. M., 1984: Slope currents and JEBAR. *J. Phys. Oceanogr.*, **14**, 795–810, doi:10.1175/1520-0485(1984)014<0795:SCA>2.0.CO;2.

Huyer, A., 1983: Coastal upwelling in the California Current System. *Prog. Oceanogr.*, **12**, 259–284, doi:10.1016/0079-6611(83)90010-1.

Kaplan, D. M., and J. Largier, 2006: HF radar-derived origin and destination of surface waters off Bodega Bay, California. *Deep-Sea Res. II*, **53**, 2906–2930, doi:10.1016/j.dsr2.2006.07.012.

Kim, S. Y., 2010: Observations of submesoscale eddies using high-frequency radar-derived kinematic and dynamic quantities. *Cont. Shelf Res.*, **30**, 1639–1655, doi:10.1016/j.csr.2010.06.011.

Kirincich, A. R., and J. A. Barth, 2009: Time-varying across-shelf Ekman transport and vertical eddy viscosity on the inner-shelf. *J. Phys. Oceanogr.*, **39**, 602–620, doi:10.1175/2008JPO3969.1.

——, ——, B. A. Grantham, B. A. Menge, and J. Lubchenco, 2005: Wind-driven inner-shelf circulation off central Oregon during summer. *J. Geophys. Res.*, **110**, C10S03, doi:10.1029/2004JC002611.

——, S. J. Lentz, and J. A. Barth, 2009: Wave-driven inner-shelf motions on the Oregon coast. *J. Phys. Oceanogr.*, **39**, 2942–2956, doi:10.1175/2009JPO4041.1.

——, T. de Paolo, and E. Terrill, 2012: Improving HF radar estimates of surface currents using signal quality metrics, with application to the MVCO high-resolution radar system. *J. Atmos. Oceanic Technol.*, **29**, 1377–1390, doi:10.1175/JTECH-D-11-00160.1.

——, S. J. Lentz, J. T. Farrar, and N. K. Ganju, 2013: The spatial structure of tidal and mean circulation over the inner shelf south of Martha's Vineyard, Massachusetts. *J. Phys. Oceanogr.*, **43**, 1940–1958, doi:10.1175/JPO-D-13-020.1.

Kohut, J. T., S. M. Glenn, and R. J. Chant, 2004: Seasonal current variability on the New Jersey inner shelf. *J. Geophys. Res.*, **109**, C07S07, doi:10.1029/2003JC001963.

Lekien, F., and S. D. Ross, 2010: The computation of finite-time Lyapunov exponents on unstructured meshes and for non-Euclidean manifolds. *Chaos*, **20**, 017505, doi:10.1063/1.3278516.

——, C. Coulliette, A. J. Mariano, E. H. Ryan, L. K. Shay, G. Haller, and J. Marsden, 2005: Pollution release tied to invariant manifolds: A case study for the coast of Florida. *Physica D*, **210**, 1–20, doi:10.1016/j.physd.2005.06.023.

Lentz, S. J., 2001: The influence of stratification on the wind-driven cross-shelf circulation over the North Carolina shelf. *J. Phys. Oceanogr.*, **31**, 2749–2760, doi:10.1175/1520-0485(2001)031<2749:TIOSOT>2.0.CO;2.

——, and M. R. Fewings, 2012: The wind- and wave-driven inner-shelf circulation. *Annu. Rev. Mar. Sci.*, **4**, 317–343, doi:10.1146/annurev-marine-120709-142745.

——, ——, P. Howd, J. Fredericks, and K. Hathaway, 2008: Observations and a model of undertow over the inner continental shelf. *J. Phys. Oceanogr.*, **38**, 2341–2357, doi:10.1175/2008JPO3986.1.

Mahadevan, A., and A. Tandon, 2006: An analysis of mechanisms for submesoscale vertical motion at ocean fronts. *Ocean Modell.*, **14**, 241–256, doi:10.1016/j.ocemod.2006.05.006.

——, L. N. Thomas, and A. Tandon, 2008: Comment on "Eddy/wind interactions stimulate extraordinary mid-ocean plankton blooms." *Science*, **320**, 448, doi:10.1126/science.1152111.

McCabe, R., P. MacCready, and G. Pawlak, 2006: Form drag due to flow separation at a headland. *J. Phys. Oceanogr.*, **36**, 2136–2152, doi:10.1175/JPO2966.1.

McGillicuddy, D. J., and Coauthors, 2007: Eddy/wind interactions stimulate extraordinary mid-ocean plankton blooms. *Science*, **316**, 1021–1026, doi:10.1126/science.1136256.

McWilliams, J. C., 1985: Submesoscale, coherent vortices in the ocean. *Rev. Geophys.*, **23**, 165–182, doi:10.1029/RG023i002p00165.

Nencioli, F., C. Dong, T. Dickey, L. Washburn, and J. C. McWilliams, 2010: A vector geometry based eddy detection algorithm and its application to a high-resolution numerical model product and high-frequency radar surface velocities in the Southern California Bight. *J. Atmos. Oceanic Technol.*, **27**, 564–579, doi:10.1175/2009JTECHO725.1.

Okubo, A., 1970: Horizontal dispersion of floatable particles in the vicinity of velocity singularities such as convergences. *Deep.-Sea Res. Oceanogr. Abstr.*, **17**, 445–454, doi:10.1016/0011-7471(70)90059-8.

Olascoaga, M. J., I. I. Rypina, M. G. Brown, F. J. Beron-Vera, H. Koçak, L. E. Brand, G. R. Halliwell, and L. K. Shay, 2006: Persistent transport barrier on the west Florida shelf. *Geophys. Res. Lett.*, **33**, L22603, doi:10.1029/2006GL027800.

Parks, A. B., L. K. Shay, W. E. Johns, J. Martinez-Pedraja, and K.- W. Gurgel, 2009: HF radar observations of small-scale surface current variability in the Straits of Florida. *J. Geophys. Res.*, **114**, C08002, doi:10.1029/2008JC005025.

Pawlowicz, R., B. Beardsley, and S. Lentz, 2002: Classical tidal harmonic analysis including error estimates in MATLAB using T_TIDE. *Comput. Geosci.*, **28**, 929–937, doi:10.1016/S0098-3004(02)00013-4.

Robinson, I., 1981: Tidal vorticity and residual circulation. *Deep-Sea Res.*, **28**, 195–212, doi:10.1016/0198-0149(81)90062-5.

Rudnick, D. L., 2001: On the skewness of vorticity in the upper ocean. *Geophys. Res. Lett.*, **28**, 2045–2048, doi:10.1029/2000GL012265.

Rypina, I. I., A. R. Kirincich, R. Limeburner, and I. A. Udovydchenkov, 2014: Eulerian and Lagrangian correspondence of high-frequency radar and surface drifter data: Effects of radar resolution and flow components. *J. Atmos. Oceanic Technol.*, **31**, 945–966, doi:10.1175/JTECH-D-13-00146.1.

Sadarjoren, I. A., and F. H. Post, 2000: Detection, quantification, and tracking of vortices using streamline geometry. *Comput. Graphics*, **24**, 333–341, doi:10.1016/S0097-8493(00)00029-7.

Shcherbina, A. Y., E. A. D'Asaro, C. M. Lee, J. M. Klymak, M. J. Molemaker, and J. C. McWilliams, 2013: Statistics of vertical vorticity, divergence, and strain in a developed submesoscale turbulence field. *Geophys. Res. Lett.*, **40**, 4706–4711, doi:10.1002/grl.50919.

Signell, R. P., and W. R. Geyer, 1991: Transient eddy formation around headlands. *J. Geophys. Res.*, **96**, 2561–2575, doi:10.1029/90JC02029.

Song, Y. T., D. B. Haidvogel, and S. M. Glenn, 2001: Effects of topographic variability on the formation of upwelling centers off New Jersey: A theoretical model. *J. Geophys. Res.*, **106**, 9223–9240, doi:10.1029/2000JC000244.

Stewart, R. H., and J. W. Joy, 1974: HF radio measurements of surface currents. *Deep.- Sea Res. Oceanogr. Abstr.*, **21**, 1039–1049, doi:10.1016/0011-7471(74)90066-7.

Tilburg, C. E., 2003: Across-shelf transport on a continental shelf: Do across-shelf winds matter? *J. Phys. Oceanogr.*, **33**, 2675–2688, doi:10.1175/1520-0485(2003)033<2675:ATOACS>2.0.CO;2.

——, and R. Garvine, 2003: Three-dimensional flow in a shallow coastal upwelling zone: Alongshore convergence and divergence on the New Jersey shelf. *J. Phys. Oceanogr.*, **33**, 2113–2125, doi:10.1175/1520-0485(2003)033<2113:TFIASC>2.0.CO;2.

Weiss, J. B., 1991: The dynamics of enstrophy transfer in two-dimensional hydrodynamics. *Physica D*, **48**, 273–294, doi:10.1016/0167-2789(91)90088-Q.

Wilkin, J., 2006: The summertime heat budget and circulation of southeast New England shelf waters. *J. Phys. Oceanogr.*, **36**, 1997–2011, doi:10.1175/JPO2968.1.

Yankovsky, A. E., and D. C. Chapman, 1995: Generation of mesoscale flows over the shelf and slope by shelf wave scattering in the presence of a stable, sheared mean current. *J. Geophys. Res.*, **100**, 6725–6742, doi:10.1029/94JC03339.